Inorganic Chemistry
Article
Cite This: Inorg. Chem. XXXX, XXX, XXX−XXX
pubs.acs.org/IC

A Family of Layered Phosphates Crystallizing in a Rare Geometrical Isomer of the Phosphuranylite Topology: Synthesis, Characterization, and Computational Modeling of $A_4[(UO_2)_3O_2(PO_4)_2]$ (A = Alkali Metal) Exhibiting Intralayer Ion Exchange

Christian A. Juillerat, Emily E. Moore, Vancho Kocevski, Theodore Besmann, and Hans-Conrad zur Loye*

The Center for Hierarchical Wasteform Materials, University of South Carolina, Columbia, South Carolina 29208, United States

Supporting Information

ABSTRACT: Single crystals of eight new layered uranyl phosphates were grown from alkali chloride fluxes: $Cs_{1.4}K_{2.6}[(UO_2)_3O_2(PO_4)_2]$, $Cs_{0.7}K_{3.3}[(UO_2)_3O_2(PO_4)_2]$, $Rb_{1.4}K_{2.6}[(UO_2)_3O_2(PO_4)_2]$, $K_4[(UO_2)_3O_2(PO_4)_2]$, $K_{2.9}Na_{0.9}Rb_{0.2}[(UO_2)_3O_2(PO_4)_2]$, $K_{2.1}Na_{0.7}Rb_{1.2}[(UO_2)_3O_2(PO_4)_2]$, $Cs_{1.7}K_{4.3}[(UO_2)_5O_5(PO_4)_2]$, and $Rb_{1.6}K_{4.4}[(UO_2)_5O_5(PO_4)_2]$. All structures crystallize in the monoclinic space group, $P2_1/c$ and contain uranyl phosphate layers with alkali metals located between the layers for charge balance. Ion exchange experiments on $Cs_{0.7}K_{3.3}[(UO_2)_3O_2(PO_4)_2]$, $Rb_{1.4}K_{2.6}[(UO_2)_3O_2(PO_4)_2]$, and $K_4[(UO_2)_3O_2(PO_4)_2]$ demonstrated that Cs and Rb cations cannot be exchanged for K cations; however, K cations can be readily exchanged for Na, Rb, and Cs. Enthalpies of formation were calculated from density functional theory (DFT) and volume-based thermodynamics (VBT) for all six structures. A value for the enthalpy of formation of the phosphuranylite sheet, $[(UO_2)_3O_2(PO_4)_2]^{4-}$, was derived using single-ion additive methods coupled with VBT. DFT and VBT calculations were used to justify results of the ion exchange experiments. $Cs_{0.7}K_{3.3}[(UO_2)_3O_2(PO_4)_2]$, $Rb_{1.4}K_{2.6}[(UO_2)_3O_2(PO_4)_2]$, and $K_4[(UO_2)_3O_2(PO_4)_2]$ exhibit typical luminescence of the uranyl group.

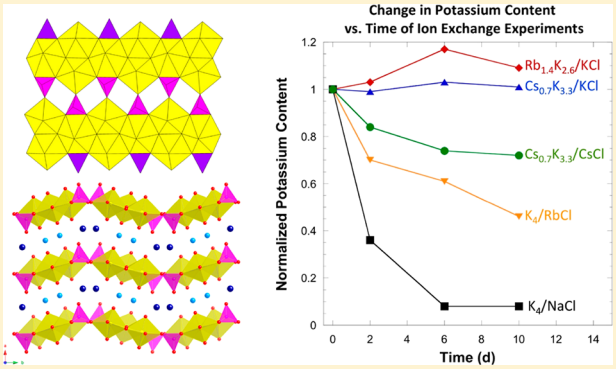

INTRODUCTION

The need to effectively immobilize radioactive waste in wasteforms that will safely endure for hundreds to thousands of years was understood from the moment that the first nuclear waste was generated.[1] Achieving this goal may require the development of multiple new waste form approaches to address specific, problematic isotopes and to effectively and safely meet the requirements for long-term storage. Particularly in the case of radioactive elements that are, or that can over time, transform into water-soluble species or air-volatile species, such as technetium or cesium, there is a clear need for custom waste forms that will maintain such isotopes in their inert oxidation states and coordination environments in the millennia to come. Layered phosphates are being suggested as potential waste forms for volatile species, such as cesium, provided they can be incorporated into the structure, either during synthesis or post-synthesis via ion exchange.

Uranium phosphates have been previously studied to investigate actinide mobility in the environment, especially in preparation for developing a long-term geological repository for nuclear waste. This is due to the prevalence of phosphate minerals in the Earth's crust and the low solubility of actinide phosphates.[2−7] We are exploring the synthesis and characterization of uranium phosphates to enhance our understanding of the potential ion exchange capacity for incorporating radioactive cesium into layered phosphates. Uranium(VI) phosphates are of particular interest, because the hexavalent state of uranium is easily accessible in a variety of systems and has a tendency to favor the formation of layered architectures. The uranyl ion, UO_2^{2+}, features strong U−O axial bonds that have short bond lengths of ∼1.80 Å, and UO_2^{2+} can equatorially coordinate with additional ligands to form square, pentagonal, and hexagonal bipyramids.[8] Typically the uranyl oxygens remain nonbonding while the equatorial bonds connect adjacent uranyl groups via corner- and edge-sharing, resulting in layered topologies.

Uranyl phosphates comprise ∼25% of all known uranyl minerals and have two dominant topologies: phosphuranylite and autunite. The autunite topology consists only of squares and is comprised of phosphate tetrahedra and uranyl square bipyramids, while the phosphuranylite topology is more diverse and is constructed of phosphate tetrahedra and pentagonal- and hexagonal-uranyl bipyramidal units. The pentagonal- and

Received: February 16, 2018

DOI: 10.1021/acs.inorgchem.8b00434
Inorg. Chem. XXXX, XXX, XXX−XXX

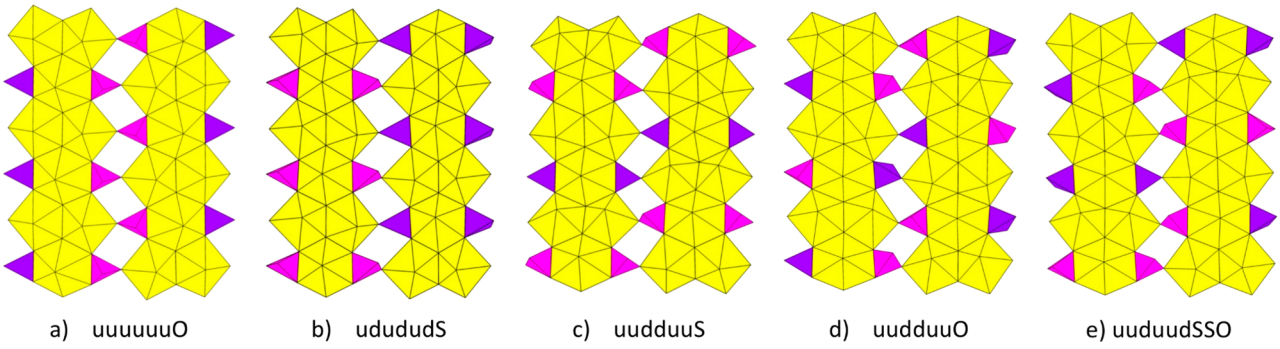

Figure 1. Five geometrical isomers of the phosphuranylite topology, where uranium polyhedra are yellow, phosphate tetrahedra in the up orientation are pink, and phosphate tetrahedra in the down orientation are purple. Examples of compounds exhibiting these isomers are (a) the materials in this work, (b) vanmeersscheite,[11] (c) phosphuranylite,[12] (d) phurcalite,[13] and (e) bergenite.[9]

Table 1. Reactant Amounts in mmol Used for the Synthesis of the Six Title Compounds

	Reactant Amount (mmol) ($A_4[(UO_2)_3O_2(PO_4)_2]$ (A = alkali metal))					
A_4	$Cs_{1.4}K_{2.6}$ (**1**)	$Cs_{0.7}K_{3.3}$ (**2**)	$Rb_{1.4}K_{2.6}$ (**3**)	K_4 (**4**)	$K_{2.1}Na_{0.7}Rb_{1.2}$ (**5**)	$K_{2.9}Na_{0.9}Rb_{0.2}$ (**6**)
UF_4	0.5	0.5	0.5	0.5	0.5	0.5
$AlPO_4$	2	0.33	0.33	0.33	0.33	0.33
CsCl	20	20				
RbCl			20		10	
KCl	4	20	20	20	10	20

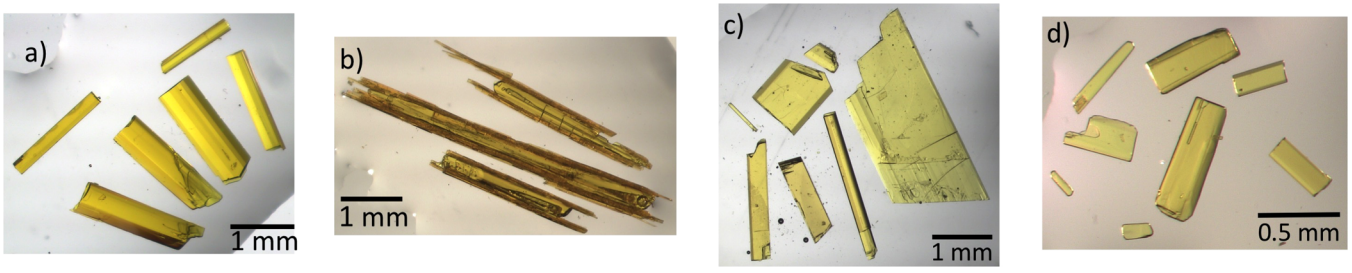

Figure 2. Selected crystal pictures of (a) $Cs_{0.7}K_{3.3}[(UO_2)_3O_2(PO_4)_2]$, (b) the intergrowth of $Cs_{1.4}K_{2.6}[(UO_2)_3O_2(PO_4)_2]$ and $Cs_{1.7}K_{4.3}[(UO_2)_5O_5(PO_4)_2]$, (c) $K_4[(UO_2)_3O_2(PO_4)_2]$, and (d) $K_{2.1}Na_{0.7}Rb_{1.2}[(UO_2)_3O_2(PO_4)_2]$.

hexagonal-uranyl bipyramids edge share to form chains that are connected together by edge- and corner-sharing phosphate tetrahedra.[3] Within the phosphuranylite class, there are four geometric isomers that occur in minerals,[9] and a fifth that has been reported in a uranyl arsenate, $K_4[(UO_2)_3O_2(AsO_4)_2]$.[10] These geometric isomers primarily differ by the orientations of the phosphate (or other nonsheet ligand) tetrahedra. Historically, such layered phosphates have been described by looking at the chains of phosphate tetrahedra and the pair of tetrahedra that edge share with the hexagonal uranyl bipyramid. For example, in vanmeersscheite[11] (Figure 1), the tetrahedra point up−down up−down up−down (ududud) and each pair of tetrahedra that are attached to the hexagonal uranyl bipyramid have the same orientation (S = same) with udududS as the overall description of the isomer. The other three geometric isomers of the phosphuranylite sheet anion topology are uudduuSS, uudduuO (O = opposite), and uudduudSSO, where the pairs of tetrahedra vary in a same−same−opposite sequence.[9,12,13] The most recent isomer reported, uuuuuuO (Figure 1) was first observed in $K_4[(UO_2)_3O_2(AsO_4)_2]$ and is the isomer of all six of the compounds reported herein: $Cs_{1.4}K_{2.6}(PO_4)_2[(UO_2)_3O_2]$ (**1**), $Cs_{0.7}K_{3.3}[(UO_2)_3O_2(PO_4)_2]$ (**2**), $Rb_{1.4}K_{2.6}[(UO_2)_3O_2(PO_4)_2]$ (**3**), $K_4[(UO_2)_3O_2(PO_4)_2]$ (**4**), $K_{2.9}Na_{0.9}Rb_{0.2}[(UO_2)_3O_2(PO_4)_2]$ (**5**), and $K_{2.1}Na_{0.7}Rb_{1.2}[(UO_2)_3O_2(PO_4)_2]$ (**6**). These six new layered uranyl phosphates are the first phosphates to adopt this particular geometric isomer. In this paper, we report on the synthesis, structure, physical characterization, ion exchange behavior, and modeling of these materials.

EXPERIMENTAL SECTION

UF_4 (International Bio-Analytical Industries, powder, ACS grade), $AlPO_4$ (Alfa Aesar, powder, 99.99%), CsCl (Alfa Aesar, powder, 99%), NaCl (Fisher Chemical, powder, 99.0%), KCl (Mallinckrodt Chemicals, powder, 99.6%), and RbCl (Alfa Aesar, powder, 99.8%) were used as received. ***Caution!*** *Although the uranium precursor used contained depleted uranium, standard safety measures for handling radioactive substances must be followed.*

Six phases were synthesized by molten flux crystal growth methods using alkali chloride fluxes.[14,15] They were numerically labeled as follows: $Cs_{1.4}K_{2.6}[(UO_2)_3O_2(PO_4)_2]$ (**1**), $Cs_{0.7}K_{3.3}[(UO_2)_3O_2(PO_4)_2]$ (**2**), $Rb_{1.4}K_{2.6}[(UO_2)_3O_2(PO_4)_2]$ (**3**), $K_4[(UO_2)_3O_2(PO_4)_2]$ (**4**), $K_{2.9}Na_{0.9}Rb_{0.2}[(UO_2)_3O_2(PO_4)_2]$ (**5**), and $K_{2.1}Na_{0.7}Rb_{1.2}[(UO_2)_3O_2(PO_4)_2]$ (**6**). For each reaction, 0.5 mmol of UF_4, 0.33 mmol of $AlPO_4$, and 20 or 40 mmol of a single-alkali or mixed-alkali chloride flux (details are given in Table 1) were loaded into 5 mL alumina crucibles measuring 2.6 mm in height and 1.8 mm in diameter. The vessels were loosely covered by alumina caps or contained in a ceramic holder (see Figure S1 in the Supporting Information) with a larger inverted alumina crucible placed over the

DOI: 10.1021/acs.inorgchem.8b00434
Inorg. Chem. XXXX, XXX, XXX−XXX

Table 2. Crystallographic Data and Information for All Six Compounds

	$A_4[(UO_2)_3O_2(PO_4)_2]$ (A = alkali metal)						$A_6[(UO_2)_5O_5(PO_4)_2]$	
	$Cs_{1.4}K_{2.6}$ (**1**)	$Cs_{0.7}K_{3.3}$ (**2**)	$Rb_{1.4}K_{2.6}$ (**3**)	K_4 (**4**)	$K_{2.1}Na_{0.7}Rb_{1.2}$ (**5**)	$K_{2.9}Na_{0.9}Rb_{0.2}$ (**6**)	$Cs_{1.7}K_{4.3}$	$Rb_{1.6}K_{4.4}$
space group	$P2_1/c$	$P2_1/c$	$P2_1/c$	$P2_1/c$	$P2_1/c$	$P2_1/c$	$P2_1/c$	$P2_1/c$
a (Å)	6.9655(3)	6.8606(2)	6.8135(2)	6.75192(2)	6.7192(2)	6.6360(2)	7.0126(3)	6.8805(2)
b (Å)	16.9723(7)	16.8937(5)	16.8886(4)	16.8422(5)	16.8408(6)	16.7983(5)	24.4238(11)	24.3128(8)
c (Å)	7.0553(3)	7.0480(2)	7.0489(2)	7.0430(2)	7.0270(2)	7.0181(2)	7.0677(3)	7.0604(2)
β (°)	99.458(2)	99.3280(10)	99.477(1)	99.9970(10)	99.9970(10)	100.0900(10)	99.157(2)	99.3290(10)
V (Å^3)	822.74(6)	806.07(4)	800.05(4)	789.32(4)	783.08(4)	770.23(4)	1192.09(9)	1165.47(6)
crystal size (mm^3)	0.05 × 0.02 × 0.01	0.05 × 0.04 × 0.01	0.08 × 0.01 × 0.01	0.08 × 0.04 × 0.01	0.03 × 0.03 × 0.01	0.04 × 0.04 × 0.02	0.1 × 0.01 × 0.01	0.04 × 0.02 × 0.01
temperature (K)	299.99	300.01	299.97	300.02	300.02	300.01	302.48	300.02
density (g cm^{-3})	5.342	5.169	5.202	5.000	5.220	5.099	5.588	5.493
θ range (deg)	2.400−36.332	2.411−36.359	2.412−36.349	3.170−36.384	2.419−36.385	3.118−36.348	3.036−36.341	3.000−36.365
μ (mm^{-1})	33.512	32.759	35.461	32.038	35.401	33.285	37.248	38.915
Data Collection and Refinement								
collected reflections	49879	75271	39787	73212	78627	76867	122488	119091
unique reflections	3996	3921	3878	3837	3807	3728	5799	5665
R_{int}	0.0325	0.0558	0.0359	0.0392	0.0411	0.0373	0.0402	0.0561
h	$-11 \le h \le 11$	$-11 \le h \le 11$	$-11 \le h \le 11$	$-11 \le h \le 11$	$-11 \le h \le 11$	$-11 \le h \le 11$	$-11 \le h \le 11$	$-11 \le h \le 11$
k	$-28 \le k \le 28$	$-28 \le k \le 28$	$-28 \le k \le 28$	$-28 \le k \le 28$	$-28 \le k \le 28$	$-11 \le k \le 11$	$-40 \le k \le 40$	$-40 \le k \le 40$
l	$-11 \le l \le 11$	$-11 \le l \le 11$	$-11 \le l \le 11$	$-11 \le l \le 11$	$-11 \le l \le 11$	$-11 \le l \le 11$	$-11 \le l \le 11$	$-11 \le l \le 11$
$\Delta\rho_{max}$ (e Å^{-3})	3.146	3.250	2.674	1.329	1.900	0.935	4.415	4.012
$\Delta\rho_{min}$ (e Å^{-3})	−2.100	−2.239	−2.004	−0.932	−0.941	−1.095	−2.919	−2.452
goodness of fit, GoF	1.117	1.058	1.165	1.170	1.096	1.116	1.082	1.078
extinction coefficient	0.00024(4)		0.00059(5)	0.00078(6)	0.00011(4)	0.00065(5)	0.00019(2)	0.00030(3)
$R_1(F)$ for $F_0^2 > 2\sigma(F_0^2)$[a]	0.0181	0.0232	0.0188	0.0122	0.0148	0.0117	0.0165	0.0213
$R_w(F_0^2)$[b]	0.0389	0.0573	0.0358	0.0275	0.0311	0.0257	0.0355	0.0505

[a] $R_1 = \sum||F_0| - |F_c||/\sum|F_0|$. [b] $wR_2 = [\sum w(F_0^2 - F_c^2)^2/\sum w(F_0^2)^2]^{1/2}$; $P = (F_0^2 + 2F_c^2)/3$; $w = 1/[\sigma^2(F_0^2) + (0.0130P)^2 + 3.5983P]$ for $Cs_{1.4}K_{2.6}[(UO_2)_3O_2(PO_4)_2]$, $w = 1/[\sigma^2(F_0^2) + (0.0305P)^2 + 2.2262P]$ for $Cs_{0.7}K_{3.3}[(UO_2)_3O_2(PO_4)_2]$, $w = 1/[\sigma^2(F_0^2) + (0.0088P)^2 + 2.2169P]$ for $Rb_{1.4}K_{2.6}[(UO_2)_3O_2(PO_4)_2]$, $w = 1/[\sigma^2(F_0^2) + (0.0082P)^2 + 1.0361P]$ for $K_4[(UO_2)_3O_2(PO_4)_2]$, $w = 1/[\sigma^2(F_0^2) + (0.0120P)^2 + 1.0409P]$ for $K_{2.1}Na_{0.7}Rb_{1.2}[(UO_2)_3O_2(PO_4)_2]$, $w = 1/[\sigma^2(F_0^2) + (0.0080P)^2 + 0.9326P]$ $K_{2.9}Na_{0.9}Rb_{0.2}[(UO_2)_3O_2(PO_4)_2]$, $w = 1/[\sigma^2(F_0^2) + (0.0118P)^2 + 5.0618P]$ for $Cs_{1.7}K_{4.3}[(UO_2)_5O_5(PO_4)_2]$, and $w = 1/[\sigma^2(F_0^2) + (0.0236P)^2 + 4.3252P]$ for $Rb_{1.6}K_{4.4}[(UO_2)_5O_5(PO_4)_2]$.

DOI: 10.1021/acs.inorgchem.8b00434
Inorg. Chem. XXXX, XXX, XXX−XXX

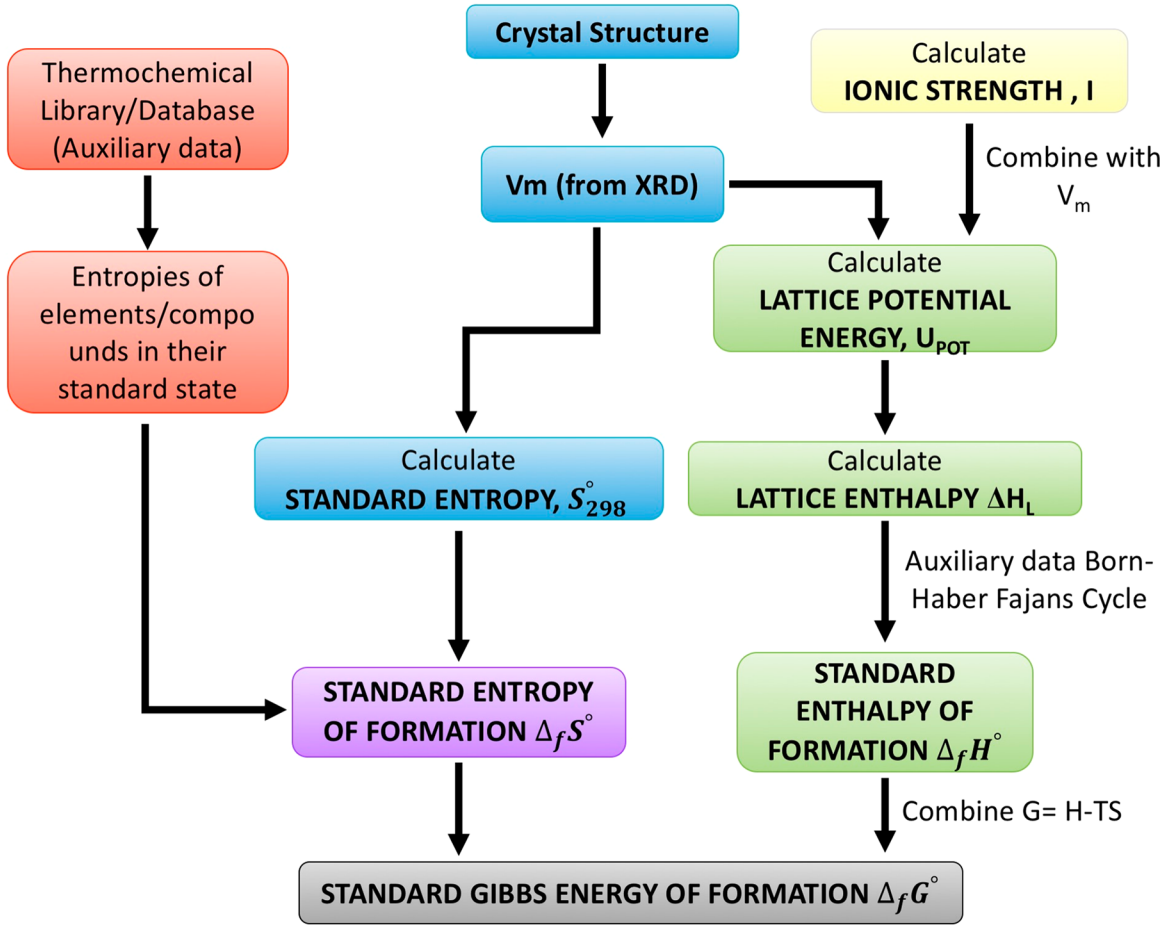

Figure 3. Description of correlations derived from crystallographic data relating auxiliary information to calculated thermodynamic values via VBT.

smaller crucible to eliminate flux volatility issues. The samples were heated to 875 °C over 1.5 h, held for 12 h, and then slowly cooled to 400 °C at a rate of 6 °C/h. The samples were sonicated in water to aid in the dissolution of the flux, and 1−2 mm yellow rods and plates of the product were obtained (see Figure 2). The yellow crystalline product grows among an orange phase identified as $Cs_{1.7}K_{4.3}[(UO_2)_5O_5(PO_4)_2]$ (**7**) and $Rb_{1.6}K_{4.4}[(UO_2)_5O_5(PO_4)_2]$ (**8**) by single-crystal X-ray diffraction (SXRD).

Structure. Structure determinations for **1**−**8** were performed using a Bruker D8 Quest single-crystal X-ray diffraction (SXRD) system that was equipped with a Mo Kα microfocus source (λ = 0.71073 Å). For products **1**−**6**, small crystals cut from thin rectangular yellow plates were used; for **7** and **8**, crystals that were used for collection were cut from orange needles. Data collection covered 99.8%−100% of the reciprocal space, up to $2\theta_{max}$ = 36.3°, with an average redundancy >10, and after absorption correction, R_{int} = 0.0325—0.0558. The raw data were reduced and corrected for absorption effects using SAINT+ and SADABS programs within the APEX 3 software.[16] The SHELXT solution program, which is an intrinsic phasing solution method, was used to obtain an initial structure that was refined using the SHELXL program.[17,18] Both SHELXT and SHELXL were used within the Olex 2 GUI.[19] Full crystallographic data can be found in Table 2.

For **1**−**8**, all atoms were refined with anisotropic displacement parameters. Free refinements of the site occupancy factors were performed on all metal atoms and showed no significant deviations from full occupancy for the U and P atoms; however, free refinements of the alkali-metal sites indicated mixed occupancy by more than one alkali metal that was confirmed by EDS. Each alkali-metal site was constrained to full occupancy by the mixed alkali elements. In **4**, free refinements of the K-site showed no significant deviation from full occupancy. For **1**−**6**, a physically reasonable structure solution was obtained in the centrosymmetric space group, $P2_1/c$. The final structure was checked using the ADDSYM program in PLATON, which found no missed symmetry elements.[20] In the $P2_1/c$ space group, structures **1**−**6** have asymmetric units containing 2 U sites, 1 P site, 8 O sites (some are split into A and B), and 2 alkali-metal sites. U(2) is at the origin with Wyckoff symbol 2*a* and symmetry $\bar{1}$, while all other sites lie on general positions with Wyckoff symbol 4*e*. For structures **7** and **8**, the asymmetric unit has 3 U sites, 1 P site, 12 O sites, and 3 alkali-metal sites. U(1) lies on Wyckoff site 2*a* with symmetry $\bar{1}$, O11 lies on 2*c* with $\bar{1}$ symmetry, and all other sites lie on general positions.

For **5** and **6**, the O6 site had large anisotropic displacement parameters, resulting in prolate O sites, and splitting this site into two produced oblate O sites with occupancies of 0.54(4) O6A, 0.46(4) O6B and 0.56(9) O6A, 0.44(9) O6B, for **5** and **6**, respectively. In **5**, the O8 site was also prolate and had large anisotropic displacement parameters; splitting the site resulted in oblate O sites with occupancies of 0.51(8) O8A and 0.49(8) O8B.

Powder X-ray Diffraction (PXRD). Powder X-ray diffraction (PXRD) data were obtained on each of the three phase-pure samples (**2**, **3**, and **4**) and on ion-exchange products. For the phases, ground samples were packed into a sample well and data were collected on a Bruker D2 Phaser equipped with an LYNXEYE silicon strip detector and a Cu Kα source. For the ion-exchange products, samples were placed onto a silicon zero background slide, and data were collected on a Rigaku Ultima IV diffractometer with a Cu Kα source and a D/teX detector. The PXRD patterns were used for product identification and to confirm sample purity.

Energy-Dispersive Spectroscopy (EDS). The presence of the appropriate elements in each of the materials was confirmed by data collected on a TESCAN Vega-3 SBU equipped with an EDS detector. Qualitatively, EDS confirmed the presence of the expected elements

DOI: 10.1021/acs.inorgchem.8b00434
Inorg. Chem. XXXX, XXX, XXX−XXX

and did not show any indication of the presence of other elements, such as F, Cl, Ag, or Al.

Optical Properties. UV-vis diffuse reflectance data were collected using a PerkinElmer Lambda 35 UV/vis scanning spectrometer that was equipped with an integrating sphere. Diffuse reflectance data were internally converted to absorbance using the Kubelka–Munk equation.[21] Fluorescence data were collected using a PerkinElmer LS55 luminescence spectrometer by first exciting at 365 nm to determine the appropriate excitation peak, then using the peak from the excitation spectrum to collect another emission spectrum. Typically, the excitation wavelength was ~525 nm and the emission wavelength was ~340 or 412 nm.

Ion Exchange. Ion-exchange experiments were performed by soaking 30 mg of ground crystalline samples of $Cs_{0.7}K_{3.3}[(UO_2)_3O_2(PO_4)_2]$ (**2**), $Rb_{1.4}K_{2.6}[(UO_2)_3O_2(PO_4)_2]$ (**3**), and $K_4[(UO_2)_3O_2(PO_4)_2]$ (**4**) in ~4 mL concentrated salt solutions in a 1 dram vial. $Cs_{0.7}K_{3.3}[(UO_2)_3O_2(PO_4)_2]$ was soaked in 11 M CsCl and 4 M KCl solutions, $Rb_{1.4}K_{2.6}[(UO_2)_3O_2(PO_4)_2]$ in 4 M KCl, and $K_4[(UO_2)_3O_2(PO_4)_2]$ in 7 M RbCl and 6 m NaCl solutions. The vials were heated in a mineral oil bath, without stirring, at 90 °C for 2–10 days before centrifuging, decanting, rinsing with water, and repeating the process of washing at least 4 times. The same experiments were also performed on 30 mg samples of single crystals of **2**–**4**. The ion exchange products were characterized by PXRD and EDS.

MODELING

Volume-Based Thermodynamics (VBT) Calculations. Predictive thermodynamics is a valuable technique, because it can provide guidelines for understanding the stability of newly synthesized materials. Volume-based thermodynamics (VBT) is a tool that was developed by Glasser et al. for estimating thermodynamic parameters of unanalyzed or even hypothetical materials for which experimental thermochemical data is thus lacking.[22–24] This allows for the development of a library of Gibbs energies of the new class of compounds synthesized herein and aids in understanding their relative stabilities. The method can be applied to a class of materials such as anhydrous minerals by using simple salt approximations when individual components of the system do not have reliable auxiliary information for determining a thermodynamic cycle to obtain the enthalpy or the energy of formation.[25]

The VBT correlation makes use of a well-known quantity such as the formula unit volume obtained from diffraction data in the form of cell volume divided by the number of formula units, Z. Figure 3 summarizes the methodology. The molar volume (V_m) combined with the ionic strength is used to calculate the standard entropy and lattice potential energy. VBT was used to calculate thermodynamic quantities for the synthesized and ion-exchanged uranyl phosphates. The entropy is calculated from eq 1, where the constants (k = 1262 and c = 13) are derived for known mineral phases[26] and the standard entropy of formation is calculated from the auxiliary data[27–30] in Table S1 in the Supporting Information.

$$S^{\circ}_{298.15} = kV_m + c \tag{1}$$

The lattice potential (U_{pot}) was calculated using eq 2 from the ionic strength ($2I$ = 42) of the individual components, i.e., phosphate and uranyl ions and other cations and anions that comprise the structure of these layered uranyl phosphates, where A is the standard electrostatic Madelung constant (121.39 kJ/mol).[22,23]

$$U_{pot} = AI\left(\frac{2I}{V_m}\right)^{1/3} \tag{2}$$

Equation 3 converts the lattice potential to a useable enthalpic value, using the number of ion types (s_i) and a constant (c_i) that is related to whether the ion is monatomic or polyatomic (linear/nonlinear).

$$\Delta H_L = U_{pot} + \sum_{i=1}^{n} s_i\left(\frac{c_i}{2} - 2\right)RT \tag{3}$$

This value allows for the calculation of the standard enthalpy of formation through the Born–Haber–Fajans cycle in which the constituents of the compounds are broken down into their gaseous ionic components and the reaction energy is calculated by summation of the energy from the gas state and the lattice potential resulting in the energetics of formation of the solid. Gaseous components from the solid phase are obtained from the auxiliary information in Table S1 in the Supporting Information and are sublimation (ΔH_{sub}) or dissociation (ΔH_{dis}) enthalpies, combined with ionization potentials (IP) or electron affinities (EA) for cationic or anionic species, respectively.

$$\Delta_f H^{\circ}_{298.15} = \Delta H_{sub} + IP + \Delta H_{dis} + EA + \Delta H_L \tag{4}$$

Finally, the Gibbs energy of formation ($\Delta_f G$) is calculated by combining the standard enthalpy and entropy of formation:

$$\Delta_f G^{\circ}_{298.15} = \Delta_f H^{\circ}_{298.15} + T\Delta_f S^{\circ}_{298.15} \tag{5}$$

The mixing entropy is calculated to account for the influence of the various alkali-metal layers, where the contribution due to mixing is greater for the partially occupied cation layers. The following expression for the mixing entropy is used, where n is the number of moles, R is the ideal gas constant, and x_i is the mole fraction of each constituent.

$$S_{mix} = -nR\sum_i x_i \ln(x_i) \tag{6}$$

Energetics of ion exchange reactions can be similarly calculated using VBT.[31] (see Figure S6 in the Supporting Information for a thermochemical reaction cycle of aqueous ion exchange). In this case, the lattice potential is used, along with the enthalpy difference for the aqueous alkali metals, i.e., essentially the hydration enthalpy of the elements. These reaction enthalpies are used to predict the feasibility of ion exchange for these phosphuranylite-based structures.

First-Principles Calculations. We performed first-principles calculations using density functional theory (DFT) via the Vienna Ab-initio Simulation Package (VASP) pseudopotential code,[32,33] with the Perdew–Burke–Ernzerhof (PBE) generalized-gradient approximation,[34] employing the projector augmented plane wave (PAW) method.[35,36] The energy cutoff for the plane wave basis expansion was set to 520 eV, and the convergence criteria for the total energies and the ionic forces was set to 10^{-4} eV and 10^{-3} eV/Å, respectively. We used a 6 × 2 × 6 Monkhorst–Pack k-mesh, which was shown to give converged total energies. To consider the magnetic properties of uranium and to capture the correlated nature of uranium 5f electrons, we performed spin-polarized calculations and used the DFT+U method.[37,38] Considering that the U atoms are surrounded by O atoms, we chose a value of U_{eff} = 4.0 eV, which is a U_{eff} value that is close to that obtained from relating experimental results for UO_2[39,40] and has been proven to reproduce the structural parameters and band gaps of for UO_3 polymorphs well.[41–43] Every cell was fully relaxed, i.e., cell volume, cell shape, and ionic positions.

DOI: 10.1021/acs.inorgchem.8b00434
Inorg. Chem. XXXX, XXX, XXX–XXX

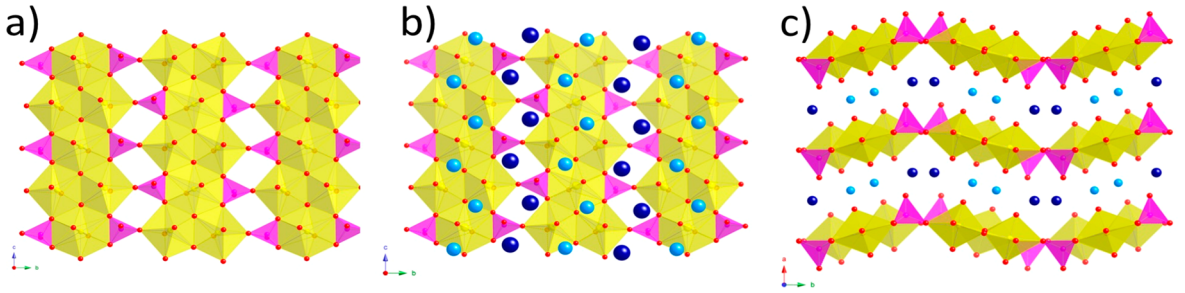

Figure 4. (a) Layer topology representative of phosphuranylite layers, $[(UO_2)_3O_2(PO_4)_2]^{4-}$, in structures **1**–**6**. (b) A layer of alkali cations added to the uranyl phosphate layer. (c) Depiction of the stacking of the layers in the *a*-direction in isostructural $Cs_{1.4}K_{2.6}[(UO_2)_3O_2(PO_4)_2]$, $Cs_{0.7}K_{3.3}[(UO_2)_3O_2(PO_4)_2]$, and $Rb_{1.4}K_{2.6}[(UO_2)_3O_2(PO_4)_2]$. The other three compositions have slight variations depicted in Figure S3 in the Supporting Information. Uranium polyhedra are yellow, phosphate tetrahedra are magenta, the larger alkali site is dark blue, the smaller site is light blue, and oxygen atoms are red.

We used the DFT-calculated total energies to calculate the enthalpies of formation, $\Delta_f H$, using the equation

$$\Delta_f H = E_{tot} - \sum_i N_i E_i \quad (7)$$

where E_{tot} is the total energy of the system and E_i is the ground state energy per atom of the element *i*. The summation is done over every atomic species *i* in the system.

RESULTS AND DISCUSSION

Synthesis. $Cs_{1.4}K_{2.6}[(UO_2)_3O_2(PO_4)_2]$ was synthesized using 0.5 mmol of UF_4, 0.33 mmol of $AlPO_4$, and 10 mmol of KCl and 10 mmol of CsCl as the flux. Under these conditions, 90% yield of a mixed-phase product was obtained, consisting of orange needles of $Cs_{1.7}K_{4.3}[(UO_2)_5O_5(PO_4)_2]$ and yellow plates of $Cs_{1.4}K_{2.6}[(UO_2)_3O_2(PO_4)_2]$, in an ~1:1 ratio. The two phases were intergrown, which made manual separation of the phases time-consuming and, at times, incomplete (see Figure 2). Altering the synthesis conditions by using twice as much flux—20 mmol of KCl and 20 mmol of CsCl—resulted in a nearly quantitative yield of, predominantly, the yellow plate phase with only small amounts of the orange phase. Interestingly, the alkali-metal composition of the yellow platelets produced under these flux-rich conditions, $Cs_{0.7}K_{3.3}[(UO_2)_3O_2(PO_4)_2]$, crystallized with a higher potassium to cesium ratio, 3.3:0.7 (K:Cs) vs 2.6:1.4, despite the fact that the ratio of Cs to K was kept the same. Attempts to modify the reaction conditions to favor the orange needle phase over the yellow phase were not successful, and, therefore, no further characterization on phases **7** and **8** was performed.

Two of the phases, $K_{2.9}Na_{0.9}Rb_{0.2}[(UO_2)_3O_2(PO_4)_2]$ (**5**) and $K_{2.1}Na_{0.7}Rb_{1.2}[(UO_2)_3O_2(PO_4)_2]$ (**6**), were obtained serendipitously, because they contain alkali metals that were not part of the original reaction mixture. It was determined that, by only loosely covering the crucibles with alumina plates, the volatile halide fluxes were able to diffuse into neighboring reaction vessels and alter the reagent mix. To prevent this from occurring in subsequent syntheses, ceramic holders with a larger inverted alumina crucible covering the smaller reaction vessel were used (see Figure S2 in the Supporting Information). The reaction with 20 mmol of KCl was repeated and produced the pure potassium phase, $K_4[(UO_2)_3O_2(PO_4)_2]$ with no significant impurities. Considering that all six phases possess the same uranyl phosphate sheets, it appears that by simply changing the alkali-metal mixture in the flux, one can obtain any number of complex alkali-layered-metal mixtures. However, attempts to obtain a structure in the same family with a high sodium content was not possible, and reactions always resulted in $Na_2U_2O_7$ as the major product. Furthermore, synthesis of these phases was attempted with only Cs or Rb; however, all attempts at obtaining the desired layered phases were unsuccessful.

Structure Description. $Cs_{1.4}K_{2.6}[(UO_2)_3O_2(PO_4)_2]$ (**1**), $Cs_{0.7}K_{3.3}[(UO_2)_3O_2(PO_4)_2]$ (**2**), $Rb_{1.4}K_{2.6}[(UO_2)_3O_2(PO_4)_2]$ (**3**), $K_4[(UO_2)_3O_2(PO_4)_2]$ (**4**), $K_{2.9}Na_{0.9}Rb_{0.2}[(UO_2)_3O_2(PO_4)_2]$ (**5**), and $K_{2.1}Na_{0.7}Rb_{1.2}[(UO_2)_3O_2(PO_4)_2]$ (**6**) crystallize in the monoclinic space group $P2_1/c$ with lattice parameters in the ranges of 6.6360(2) Å ≤ *a* ≤ 6.9655(3) Å, 16.7983(5) Å ≤ *b* ≤ 16.9723(7) Å, 7.0181(2) Å ≤ *c* ≤ 7.0553(3) Å, and 99.3280(10)° ≤ *β* ≤ 100.0900(10)°. Full crystallographic data for each compound can be found in Table 2, and bond valence sums and bond distances are collected in Tables S2–S7 in the Supporting Information. In the asymmetric unit, there are two U sites, one P site, eight O sites (some are split into A and B), and two alkali metal sites. All six structures have isomorphic layers, based on the phosphuranylite topology, and are comprised of phosphate tetrahedra and uranyl pentagonal and hexagonal bipyramids.[8] The UO_7 polyhedra edge-share to form U_2O_{12} dimers that edge-share with UO_8 hexagonal bipyramids to construct a chain of alternating pentagon dimers and hexagons. These chains are linked to adjacent chains by phosphate tetrahedra that corner-share and edge-share with the chains (see Figure 4a). There are several geometrical isomers in the phosphuranylite group that differ only by the orientation of the phosphate tetrahedra.[8] All six phases reported here crystallize as the same isomer. Interestingly, none of the four known geometrical isomers observed in uranyl minerals match the layers in the six compounds; however, this geometrical isomer of the phosphuranylite anion-topology has been observed in a uranyl arsenate, $K_4[(UO_2)_3O_2(AsO_4)_2]$.[10] $K_4[(UO_2)_3O_2(PO_4)_2]$ (**4**) is isostructural with $K_4[(UO_2)_3O_2(AsO_4)_2]$ and both contain fully occupied potassium sites between the phosphuranylite based layers that stack in the *a* direction. The other compositions contain phosphuranylite-based layers with unique chemical compositions, which are a function of the different constituent alkali metals.

Structures **1**, **2**, and **4**–**6** all have mixed-alkali sites, where the larger alkali metal is located between the phosphate tetrahedra, while the smaller alkali metal is located between the uranyl polyhedra. This is likely a space filling issue, since, between the layers, there is more space between the phosphate tetrahedra than between the uranyl polyhedra. For example, in the Cs/K

DOI: 10.1021/acs.inorgchem.8b00434
Inorg. Chem. XXXX, XXX, XXX–XXX

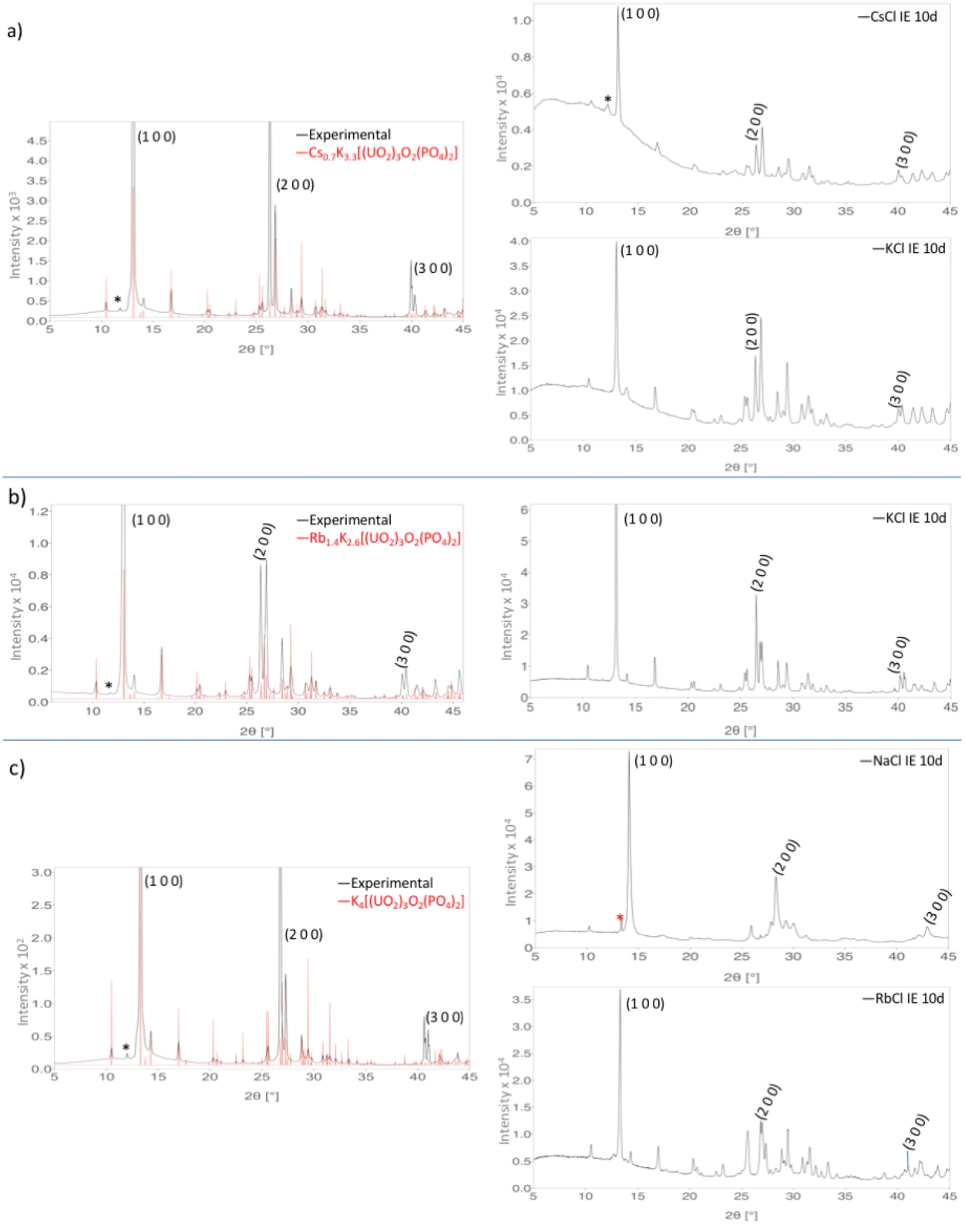

Figure 5. PXRD patterns from 5° 2θ to 45° 2θ for pure phases **2**, **3**, and **4**, and IE products. (a) PXRD of **2** on the left, and IE products of **2** soaked in CsCl and KCl on the right. (b) PXRD of **3** of the left and IE product of **3** soaked in KCl on the right. (c) PXRD of **4** on the left, and IE products of **4** soaked in NaCl and RbCl on the right. Black asterisks mark K_β peaks and the red asterisk indicates a small unidentified impurity.

and Rb/K structures, the alkali site between the phosphate tetrahedra is occupied both by Cs and K, or Rb and K, while the smaller alkali site is fully occupied by K. In the two structures with three alkali species, K/Rb occupy the larger alkali site, and K/Na occupy the smaller site. In both of these structures, $K_{2.9}Na_{0.9}Rb_{0.2}[(UO_2)_3O_2(PO_4)_2]$ (**6**) and $K_{2.1}Na_{0.7}Rb_{1.2}[(UO_2)_3O_2(PO_4)_2]$ (**5**), there is disorder in the O anions bonded to the P atom (see Figure S3 in the

DOI: 10.1021/acs.inorgchem.8b00434
Inorg. Chem. XXXX, XXX, XXX−XXX

Supporting Information). In $K_{2.9}Na_{0.9}Rb_{0.2}[(UO_2)_3O_2(PO_4)_2]$, O6, which is shared by P1 and U2, is split into two sites, O6A and O6B. O8, the phosphate oxygen that points into the layers is also split into two sites: O8A and O8B. In $K_{2.1}Na_{0.7}Rb_{1.2}[(UO_2)_3O_2(PO_4)_2]$, only O6 is split. These split positions are likely the result of having two differently sized alkali metals occupying the same crystallographic site.

The PXRD patterns in Figure 5 show good agreement between calculated and experimental patterns of products **2**, **3**, and **4**; however, the peaks do not display the expected intensities, as a consequence of extreme preferred orientation in the (1 0 0) direction of the platelet-shaped crystals. To better view the details of these patterns, the tops of the peaks in the (1 0 0) direction have been cutoff. Nevertheless, the patterns confirm pure samples of products **2**, **3**, and **4**. The PXRD patterns of the ion exchange products are also shown in Figure 5. Since the ion-exchange products were loaded onto zero background slides, instead of packed into sample wells, the preferred orientation is less severe. Also, the broad hump between 5° 2θ and 15° 2θ is due to iron fluorescence from the sample holder. All of the ion-exchanged products generate diffraction patterns similar to that of the pure starting materials, indicating that the sheet structure remains intact during the ion-exchange process and the only structural change is caused by the change in the identity of the alkali-metal cation. Not unexpectedly, some peak broadening is observed after the ion exchange, likely due to the loss of crystallinity caused by the ion-exchange process.

Structure **7** and **8** are isostructural and also crystallize in the monoclinic space group $P2_1/c$ with lattice parameters of a = 7.0126(3) Å, b = 24.4238(11) Å, c = 7.0677(3) Å, and β = 99.157(2)° for **7**, and a = 6.8805(2) Å, b = 24.3128(8) Å, c = 7.0604(2) Å, and β = 99.390(10)° for **8**. Lattice parameters a, c, and β are similar to those for structures **1**–**6**, while b is significantly larger to account for the added uranium and alkali metal sites. Figure 6 demonstrates the relationship between the

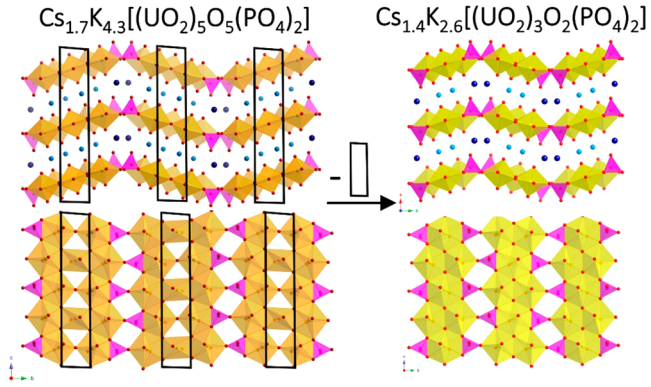

Figure 6. Relationship between the $Cs_{1.4}K_{2.6}[(UO_2)_3O_2(PO_4)_2]$ and $Cs_{1.7}K_{4.3}[(UO_2)_5O_5(PO_4)_2]$ structures is shown by the removal of two uranyl sites in the $Cs_{1.7}K_{4.3}[(UO_2)_5O_5(PO_4)_2]$ structures. Uranyl polyhedra are yellow or light orange, phosphate tetrahedra are magenta, Cs/K sites are dark blue, K is light blue, and O atoms are red.

$[(UO_2)_3O_2(PO_4)_2]^{4-}$ and the $[(UO_2)_5O_5(PO_4)_2]^{6-}$ layers. The uranyl phosphate sheet is constructed of mirror-image chains of uranyl pentagonal bipyramids that are connected by uranyl square bipyramids. These units are connected to subsequent units by edge- and corner-sharing phosphate tetrahedra. This sheet topology can be described as a combination of the uranophane and β -U_3O_8 topologies and had been previously observed in $K_6[(UO_2)_5O_5(AsO_4)_2]$, which is isostructural with **7** and **8**.[10] As seen in structures **1**–**6**, adjacent phosphate tetrahedra point in the same direction and stack in the same direction of tetrahedra in the adjacent layers, creating a larger space between the phosphate tetrahedra, compared to the uranyl polyhedra. For this reason, the alkali site directly below the phosphate tetrahedra is partially occupied by Cs/K and Rb/K accommodating the larger alkali cation, while K cations lie between uranyl polyhedra. The similarity in structure between $A_4[(UO_2)_3O_2(PO_4)_2]$ and the $A_6[(UO_2)_5O_5(PO_4)_2]$ helps explain the aggressive intergrowth of the yellow and orange phases.

Optical Properties. The fluorescence spectra for $Cs_{0.7}K_{3.3}[(UO_2)_3O_2(PO_4)_2]$ (**2**), $Rb_{1.4}K_{2.6}[(UO_2)_3O_2(PO_4)_2]$ (**3**), and $K_4[(UO_2)_3O_2(PO_4)_2]$ (**4**) are shown in Figure 7, along with optical pictures of ground crystals of $Rb_{1.4}K_{2.6}[(UO_2)_3O_2(PO_4)_2]$ taken under artificial and UV light (365 nm) are shown in Figure 8, which is representative of all three materials. All three compounds exhibit yellow-green luminescence typical of uranyl-containing materials with the most intense emission peak at ∼525 nm resulting from the electronic emission from the lowest vibrational level of the first excited state to the lowest vibrational level of the ground state.[44] There are several smaller peaks in the range of 450–600 nm, which originate from different vibrational levels of the same electronic emission. The compound with the largest interlayer spacing, $Cs_{0.7}K_{3.3}[(UO_2)_3O_2(PO_4)_2]$ (**1**), fluoresces more intensely, although visually, the intensities are indistinguishable. The UV-vis absorbance spectra for $Cs_{0.7}K_{3.3}[(UO_2)_3O_2(PO_4)_2]$ (**2**), $Rb_{1.4}K_{2.6}[(UO_2)_3O_2(PO_4)_2]$ (**3**), and $K_4[(UO_2)_3O_2(PO_4)_2]$ (**4**) are shown in Figure S4 in the Supporting Information and display broad absorbance between 200 nm and 520 nm. The band gaps are estimated to be 2.4 eV, indicating that all three materials are semiconductors.

Modeling. The model system used for the first-principles calculations was derived from the experimentally determined structures. However, except for the $K_4[(UO_2)_3O_2(PO_4)_2]$ system, all other systems have partial occupancies on the alkali cation site. Obtaining the lowest energy structure at the specific composition requires the generation of a large number of supercells, where the alkali cations on the site with partial occupancy are randomly replaced. With the $Cs_{1.4}K_{2.6}[(UO_2)_3O_2(PO_4)_2]$ system as an example, a supercell of 250 atoms (5 times larger) would be required to capture the $Cs_{1.4}K_{2.6}$ composition, with 77 520 possible combinations. Performing calculations for such a big system, and such a large number of possible combinations, is a very time-consuming and computationally demanding task. For that reason, a primitive cell with only 8 cations in 2 distinct sites was used and, by adding or removing 1 cation, the concentration of the alkali cations was changed in increments of 0.5 per formula unit. The enthalpies of formation for the systems with partial occupancies were calculated as a weighted average of the formation enthalpies of the system with the composition closest to that which has been experimentally reported. For example, if $A_xB_y[(UO_2)_3O_2(PO_4)_2]$ is the experimentally reported concentration, and $A_{x1}B_{y1}[(UO_2)_3O_2(PO_4)_2]$, and $A_{x2}B_{y2}[(UO_2)_3O_2(PO_4)_2]$ are the closest compositions with enthalpies of formation ΔH_1 and ΔH_2, respectively, the enthalpy of formation of the system with partial occupancy, $\Delta_f H_{mix}$, is from eq 8:

DOI: 10.1021/acs.inorgchem.8b00434
Inorg. Chem. XXXX, XXX, XXX−XXX

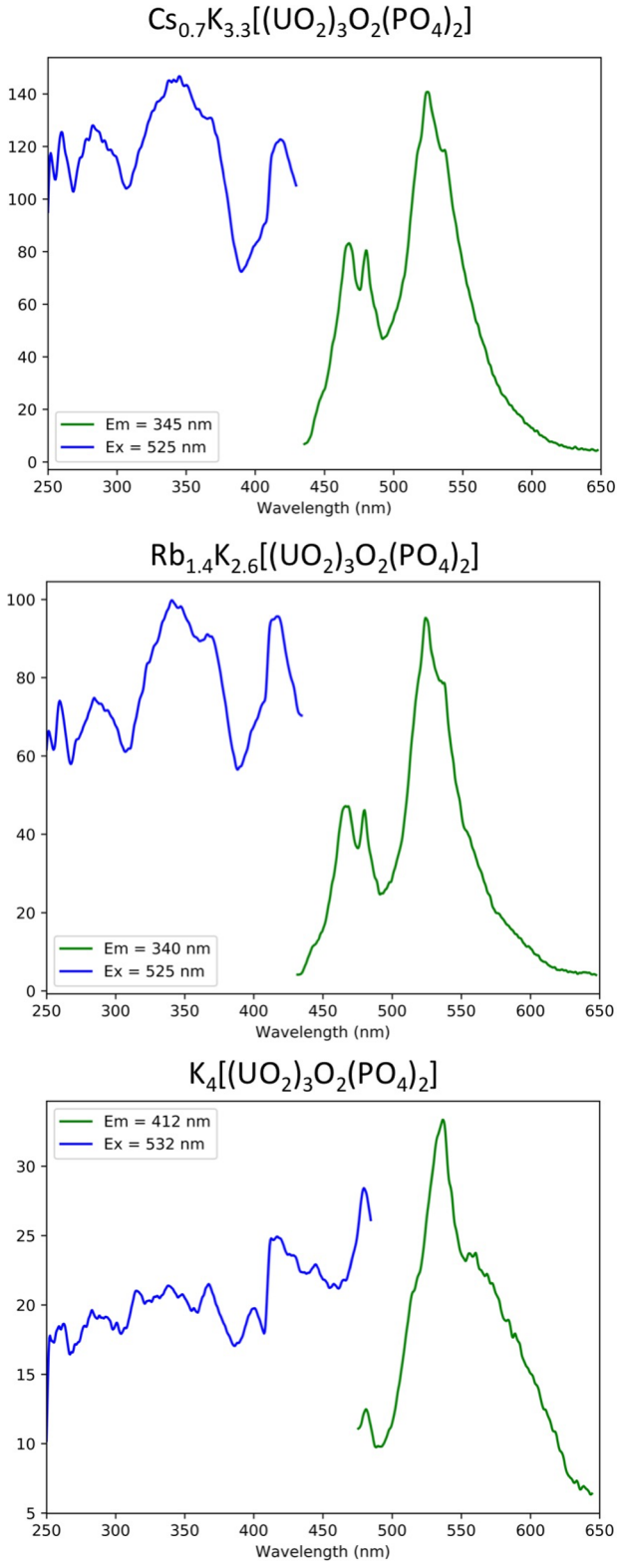

Figure 7. Fluorescence spectroscopy of selected compositions.

$$\Delta_f H = 2(x - x_1)\Delta H_1 + 2(y_2 - y)\Delta H_2 \quad (8)$$

The computed $\Delta_f H$ values are listed in Table 4 (shown later in this work) for the various alkali-metal compositions. However, note that calculations using DFT values are for 0 K, whereas to obtain the Gibbs energy at higher temperatures, we need to determine the entropy. Unfortunately, evaluation of the necessary vibrational and configurational entropy requires the phonon density of states, and considering the large system size with low symmetry, such phonon calculations would be very computationally demanding and beyond the scope of this study.

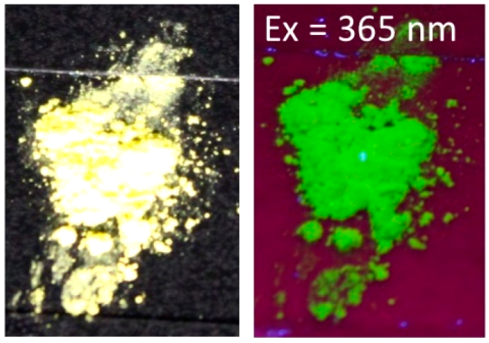

Figure 8. Luminescence of $Rb_{1.4}K_{2.6}[(UO_2)_3O_2(PO_4)_2]$ at an excitation wavelength of 365 nm, representative of all structures.

For VBT, the molar volumes (V_m) are derived from the SXRD data found in Table 2 by dividing the cell volume by the number of formula units per cell. Calculations of the standard entropy and lattice potential energy obtained using eqs 1 and 2, respectively, employ the calculated V_m values. These are summarized in Table 3 for each of the layered phosphate structures. Thermochemical cycles were constructed from the results to obtain the enthalpy of formation of each compound. The cycle (Born–Haber–Fajans) is strictly dependent on the auxiliary data available in the literature, which can be limiting. In this case, information on the gaseous phosphate anion is replaced by that of phosphorus oxide with a single negative charge, because there are no thermodynamic data available for the formation of PO_4^{3-} (g). Consequently, various oxidation states of the uranyl cation must be considered, as well as available data for the electron affinity for the oxygen anion to charge balance the compound. Therefore, we have chosen to use the cycle observed in Figure 9 for the calculation of the enthalpies of formation with the auxiliary data of Table S1.

Table 3. Molar Volumes from XRD, Entropy, and Lattice Potential from Molar Volume

A_4	V_m (A^3)	S (J/mol/K)	U_{pot} (kJ/mol)
$Cs_{1.4}K_{2.6}$	411.4	532	11914
$Cs_{0.7}K_{3.3}$	403.0	522	11996
$Rb_{1.4}K_{2.6}$	400.0	518	12026
K_4	394.7	511	12080
$K_{2.1}Na_{0.7}Rb_{1.2}$	391.5	507	12112
$K_{2.9}Na_{0.9}Rb_{0.2}$	385.1	499	12179

The resulting values for the enthalpy of formation of each layered uranyl phosphate computed by VBT are compared to those from DFT in Table 4. The derived Gibbs energies of formation using eq 5, which are calculated with $S^\circ_{298.15}$ from VBT and auxiliary data to arrive at the standard entropy of formation and include the mixing entropy due to the different cationic species, eq 6 are also given for reference in Table 4. The VBT enthalpy values are used as a benchmark comparison to DFT, although they cannot be exactly compared as, again, the latter values are calculated at 0 K, and thus caution must be taken when comparing their relative orders of magnitude, as temperature effects might be significant. The enthalpy and

DOI: 10.1021/acs.inorgchem.8b00434
Inorg. Chem. XXXX, XXX, XXX–XXX

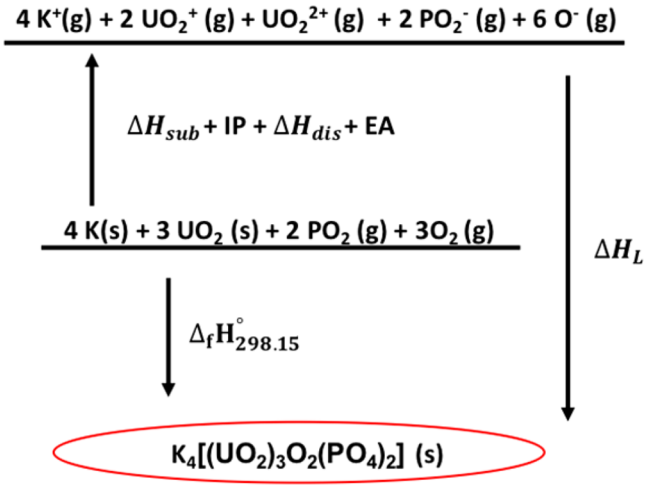

Figure 9. Born–Haber cycle used to calculate the enthalpy of formation of phosphuranylites.

Table 4. Enthalpy of Formation (from VBT and DFT), and Gibbs Energies of Formation (from VBT)

	Enthalpy of Formation (kJ/mol/formula unit)		Gibbs Energy of Formation (kJ/mol/formula unit)
A_4	$\Delta_f H^\circ_0$ (DFT)	$\Delta_f H^\circ_{298.15}$ (VBT)	$\Delta_f G^\circ_{298.15}$ (VBT)
$Cs_{1.4}K_{2.6}$	−6598	−6966	−6601
$Cs_{0.7}K_{3.3}$	−6530	−7009	−6643
$Rb_{1.4}K_{2.6}$	−6607	−7033	−6668
K_4	−6600	−7054	−6685
$K_{2.1}Na_{0.7}Rb_{1.2}$	−6586	−7048	−6686
$K_{2.9}Na_{0.9}Rb_{0.2}$	−6569	−7072	−6710

Gibbs energy of formation vary linearly with respect to V_m, (see Figure 10), where the structures with larger cations such as Cs and Rb are somewhat less stable, i.e., possess more-positive $\Delta_f G$ values. Linear regression of the data allows for the prediction of energetics, with respect to molar volume, which is largely related to cation size, as V_m is directly proportional to the average cation radius.

Extrapolation to the formation enthalpy of the phosphuranylite sheet was accomplished by applying the single-ion additive method for the alkali metals derived by Glasser et al.[17] By applying the values of the enthalpy of formation for the cations, a linear relationship in composition for the $\Delta_f H$ $[(UO_2)_3O_2(PO_4)_2]^{4-}$ sheet is observed, with values differing by 2.4%, depending on the cationic species. The average value derived for $\Delta_f H$ $[(UO_2)_3O_2(PO_4)_2]^{4-}$ = −5779 ± 50 kJ/mol, which is a value that can be compared to the enthalpy of formation of a similar compound: $(PO_4)_2(UO_2)_3$ = −5491 kJ/mol, as measured by solution calorimetry in concentrated H_2SO_4 by Cordfunke et al.[45] More recently, it has been found that phosphate compounds and minerals have proven difficult to properly fit estimated energetics of formation.[46,47] Holland et al. noted that the fitting formation enthalpies derived by the thermodynamic difference rule to experimental values of inorganic oxides (silicates, vanadates, and borates) required the exclusion of the P_2O_5 phosphates to obtain an acceptable linear regression fit.[46] Similarly, Drouet et al. was unable to find a relationship between cation size and the enthalpy of formation for apatite minerals and, instead, relied on other properties, such as electronegativity, for an acceptable fit.[47] This work is significant in that it is the first attempt to establish a value for a complex structure such as the phosphuranylite sheet, $[(UO_2)_3O_2(PO_4)_2]^{4-}$, using VBT.

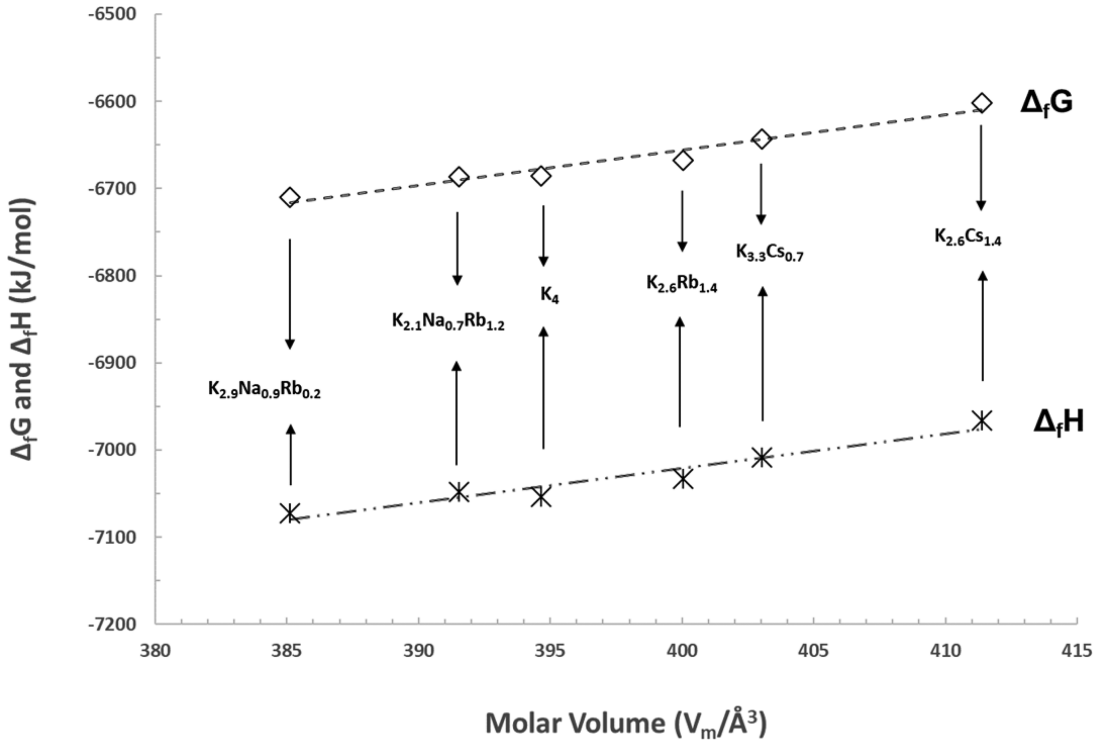

Figure 10. Graph of the enthalpy and Gibbs energy of formation, as calculated with VBT. The Gibbs energy values are calculated using the entropy of formation and entropy of mixing.

DOI: 10.1021/acs.inorgchem.8b00434
Inorg. Chem. XXXX, XXX, XXX−XXX

Ion Exchange. Successful partial ion exchange of the alkali species can be observed within as little as 2 days by examining the shift in the PXRD patterns (Figure 5) and elemental composition, as determined by EDS (Figure 11). As a

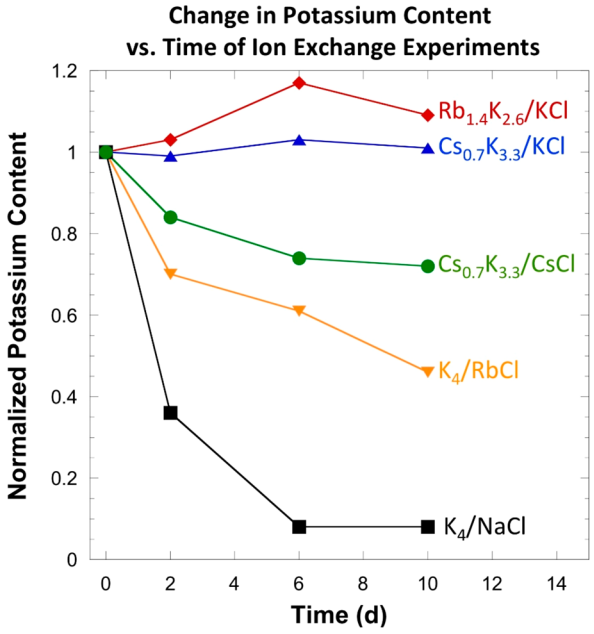

Figure 11. Graph of the normalized potassium content of powder samples during ion exchange experiments obtained from EDS results. The potassium content is normalized to the amount identified by EDS prior to ion exchange, which can differ up to 10% of the expected value, as determined from SXRD and verified by PXRD. Each experiment is identified by the initial alkali composition and the saturated salt solution used.

semiquantitative method, the EDS values can reasonably be treated with ~10% relative uncertainty. The pure K phase was soaked in RbCl and NaCl solutions and resulted in final compositions of $Rb_{1.1}K_{2.9}$ and $K_{0.3}Na_{3.7}$, respectively, as determined by EDS. (Hereafter, we will refer to the phases by just the alkali composition.) No significant change in alkali composition was detected in the experiments soaking $Cs_{0.7}K_{3.3}$ and $Rb_{1.4}K_{2.6}$ in KCl, suggesting that it is unfavorable for the larger alkali metals (Cs and Rb) to exchange with K. This is desirable for potential waste form materials, since cesium is one of the daughter products contained in nuclear waste. By soaking the $Cs_{0.7}K_{3.3}$ composition in CsCl, a final composition of $Cs_{1.9}K_{2.1}$ was obtained after 10 days, suggesting that the opposite, however, can occur with the exchange of K by Cs. The experiments run on single crystals resulted in a loss of crystallinity too severe to obtain a structure solution by SXRD, but when ground and examined as powder samples, yielded results consistent with those obtained from the powder ion-exchange experiments.

The enthalpies of formation calculated using DFT for compounds **1**–**6** detailed in Table 4 provide for relative stabilities. To estimate the enthalpies for ion exchange, we also calculated the enthalpies of formation for the ion-exchange products ($Cs_{1.9}K_{2.1}$, $Rb_{1.1}K_{2.9}$, and $K_{0.3}Na_{3.7}$), as well as the total energy for isolated alkali ions;[48] the results are shown in Tables S13 and S14 in the Supporting Information. Using the enthalpies of formation and the total energies of isolated ions, we calculated the ion-exchange energies, $\Delta_{ie}E$, using the equation

$$\Delta_{ie}E = E^{p}_{tot} + nE^{ex} - E^{r}_{tot} - nE^{in} \quad (9)$$

where E^{p}_{tot} and E^{r}_{tot} are the total energies of the ion exchange product and reactant, respectively; E^{ex} and E^{in} are the total energies of the exchanged and inserted ions; and n is the number of exchanged ions. The ion-exchange energies calculated from DFT are summarized in Table S15 in the Supporting Information. Evidently, exchanging the K^+ ions, from K_4, with Na^+ ions to form $K_{0.3}Na_{3.7}$ compound and exchanging K^+ ions, from $Cs_{0.7}K_{3.3}$, with Cs^+ ions to form $Cs_{1.9}K_{2.1}$ compound are favorable processes, indicated by the negative ion-exchange energies. However, we obtain a positive ion exchange energy for the exchange of the K^+ ions from K_4 with Rb^+ ions to form the $Rb_{1.1}K_{2.9}$ compound, meaning that the formation of $Rb_{1.1}K_{2.9}$ composition from K_4 is thermodynamically unfavorable. Generally, the DFT calculations show that exchanging K^+ ions with larger ions (Rb^+ and Cs^+) is an unfavorable process, whereas exchanging K^+ with Na^+ is favorable. The fact that the current DFT calculations include neither the hydration enthalpy of the system and the ions nor the effect of temperature above 0 K may explain the discrepancy between the DFT and experimental results for the $Rb_{1.1}K_{2.9}$ composition and the ion exchange between K^+ and larger ions.

Unlike DFT, which gives the energies at 0 K in a vacuum, the VBT method of calculating ion-exchange energies makes use of the hydration energies of the cations that exchange within the layered system, as well as the lattice potential of the structure. The lattice potential of the starting material is calculated from the SXRD data, as described in Table 3, however, the lattice potential of the newly substituted (ion-exchanged) material is unknown. We can calculate this value by establishing an average molar volume of the phosphuranylite $[(UO_2)_3O_2(PO_4)_2]^{4-}$ parent ion from the known structures and substitute various alkali metals with known V_m from thermochemical radii derived from the Goldschmidt ionic radii.[49] Therefore, we are able to predict molar volumes of hypothetical layered structures for which new lattice potentials are derived and used for ion exchange, as described in the Supporting Information.

The ion-exchange reaction of alkali metals is dependent on two competing factors, both of which are size-dependent. The lattice potential of these systems is largely governed by the cations within the layers, as the system with larger ions have smaller lattice potentials (see Table 3), which plays into the stability of the compounds. However, the competing mechanisms are that, while the structures with larger ions between the layers might be inherently less stable, the larger ions have lower hydration energies, compared to their smaller counterparts. In a given aqueous solution, smaller ions such as sodium or potassium have a higher affinity for water and would therefore rather remain in solution. The VBT calculations for simply exchanging K with Na result in positive enthalpies (see Table S11 in the Supporting Information), indicating that it is not favorable, although this might be overcome by greatly increasing the Na ion concentration in the solution, possibly resulting in a new structure that is not predicted by VBT. When exchanging K with Rb, similarly positive ion-exchange enthalpies are computed, indicating this reaction to be unfavorable, although exchanging to RbK_3 has a small energy barrier, which could potentially be overcome by increasing the Rb concentration. Exchanging the partially substituted $Cs_{0.7}K_{3.3}$

DOI: 10.1021/acs.inorgchem.8b00434
Inorg. Chem. XXXX, XXX, XXX−XXX

to result in a higher Cs concentration, such as Cs_2K_2, was also calculated to have a positive enthalpy of exchange. This is due to the fact that, although the hydration energy needed to pull the K^+ into solution is thermodynamically favorable, the driving force for Cs^+ to be included in the structure ($-\Delta H_{hyd}$) is not large enough to overcome the more-stable lattice potential of the original $Cs_{0.7}K_{3.3}$ structure. A similar argument is made for the favorable VBT exchange energy to full K_4, where the higher affinity for K^+ to remain in solution cannot compete with the increased stability in lattice potential of the pure potassium phase. The difference in enthalpies for the following two ion-exchange products, $Rb_{1.1}K_{2.9}$ and $Cs_{1.9}K_{2.1}$, are relatively small (<23 kJ/mol) and could possibly become thermodynamically stable when entropic considerations at the standard state temperature of 298.15K are taken into account. VBT predicts sodium exchange to be unfavorable, and, therefore, more-detailed descriptions are necessary to support the experimental observation. Both methods use an average structure derived from the single-crystal data of the six compounds, which are relatively close in size, since they all contain potassium between the layers. A primarily sodium-containing structure was not experimentally observed, and the ionic size difference could be a significant factor impacting the DFT and VBT results.

CONCLUSIONS

Crystals of eight new uranyl phosphates were synthesized by the molten flux growth method in alkali chloride melts. The amount of flux proved important when targeting the formation of a single phase versus a mixture of phases. Increasing the relative amount of flux to reagents leads to single-phase products of **2**–**4** that could be isolated and used in the ion-exchange experiments to determine if larger alkali metals could be exchanged for smaller ones and vice versa. Potassium can be exchanged for Rb, Cs, and Na, while Cs and Rb cations are retained in the structure, which is ideal for nuclear waste storage applications. DFT and VBT methods were used to calculate enthalpies of formation for structures **1**–**6**, and, while demonstrating good agreement, further experimentally derived thermodynamic values are needed to validate these methods. In both VBT and DFT results, the differences in enthalpies between the six phases was minor (less than 2.4%), suggesting that a large range of alkali compositions between the phosphuranylite-based layers are energetically favorable. VBT methods were used to calculate the Gibbs energy of formation of each of structures **1**–**6** by incorporating the mixing entropy of the cation layers, resulting in a linear trend, with respect to V_m. The formation enthalpy of the phosphuranylite sheet, $[(UO_2)_3O_2(PO_4)_2]^{4-}$, was derived using VBT and single-ion additive methods and found to be in relative good agreement with experimental data for a similar uranyl phosphate compound. This allows for the prediction of the formation of new compounds based on this sheet structure. DFT successfully predicted the ion-exchange experiments resulting in $Na_{3.7}K_{0.3}$ and $Cs_{1.9}K_{2.1}$ products being energetically favorable. VBT predicted these same experiments to have small, positive enthalpies that could potentially be energetically favorable, once entropic terms are considered. Both DFT and VBT predicted the $Rb_{1.1}K_{2.9}$ ion-exchange product to be energetically unfavorable, in contrast to that which has been observed.

ASSOCIATED CONTENT

Supporting Information

The Supporting Information is available free of charge on the ACS Publications website at DOI: 10.1021/acs.inorgchem.8b00434.

Auxiliary thermodynamic data, bond valence sums, bond distances, PXRD patterns of pure and ion-exchanged phases from 5° 2θ to 65° 2θ; additional structure figures; UV-vis absorption data; thermochemical cycle for ion exchange calculations; molar volumes; lattice potentials; VBT ion-exchange energies; and additional DFT enthalpies of formation (PDF)

AUTHOR INFORMATION

Corresponding Author

*E-mail: zurloye@mailbox.sc.edu.

ORCID

Vancho Kocevski: 0000-0002-2127-5834

Hans-Conrad zur Loye: 0000-0001-7351-9098

Notes

The authors declare no competing financial interest.

ACKNOWLEDGMENTS

This work was supported as part of the Center for Hierarchical Waste Form Materials, an Energy Frontier Research Center funded by the U.S. Department of Energy, Office of Science, Basic Energy Sciences under Award No. DE-SC0016574. C. Juillerat is additionally supported by an NSF IGERT Graduate Fellowship, under Grant No. 1250052. V.K., E.M., and T.B. acknowledge the use of HPC clusters Bolden and Hyperion, supported by the Division of Information Technology at the University of South Carolina.

REFERENCES

(1) Kirst, W. E. *Clinton Laboratories process manual. Section 8. Waste disposal: Wet B process*; Clinton Laboratories: Wilmington, DE, 1943.

(2) Ling, J.; Wu, S.; Chen, F.; Simonetti, A.; Shafer, J. T.; Albrecht-Schmitt, T. E. Does Iodate Incorporate into Layered Uranyl Phosphates Under Hydrothermal Conditions. *Inorg. Chem.* **2009**, *48*, 10995–11001.

(3) Burns, P. C. A new uranyl phosphate chain in the structure of parsonsite. *Am. Mineral.* **2000**, *85*, 801–805.

(4) Yagoubi, S.; Renard, C.; Abraham, F.; Obbade, S. Molten salt flux synthesis and crystal structure of a new open-framework uranyl phosphate $Cs_3(UO_2)_2(PO_4)O_2$: Spectroscopic characterization and cationic mobility studies. *J. Solid State Chem.* **2013**, *200*, 13–21.

(5) Villa, E. M.; Marr, C. J.; Jouffret, L. J.; Alekseev, E. V.; Depmeier, W.; Albrecht-Schmitt, T. E. Systematic evolution from uranyl(VI) phosphites to uranium(IV) phosphates. *Inorg. Chem.* **2012**, *51*, 6548–6558.

(6) Villa, E. M.; Marr, C. J.; Diwu, J.; Alekseev, E. V.; Depmeier, W.; Albrecht-Schmitt, T. E. From Order to Disorder and Back Again: In Situ Hydrothermal Redox Reactions of Uranium Phosphites and Phosphates. *Inorg. Chem.* **2013**, *52*, 965–973.

(7) Wu, S.; Kowalski, P. M.; Yu, N.; Malcherek, T.; Depmeier, W.; Bosbach, D.; Wang, S.; Suleimanov, E. V.; Albrecht-Schmitt, T. E.; Alekseev, E. V. Highly Distorted Uranyl Ion Coordination and One/Two-Dimensional Structural Relationship in the $Ba_2[UO_2(TO_4)_2]$ (T = P, As) System: An Experimental and Computational Study. *Inorg. Chem.* **2014**, *53*, 7650–7660.

(8) Burns, P. C. U^{6+} minerals and inorganic compounds: Insights into an expanded structural hierarchy of crystal structures. *Can. Mineral.* **2005**, *43*, 1839–1894.

DOI: 10.1021/acs.inorgchem.8b00434
Inorg. Chem. XXXX, XXX, XXX–XXX

(9) Locock, A. J.; Burns, P. C. The crystal structure of bergenite, a new geometrical isomer of the phosphuranylite group. *Can. Mineral.* **2003**, *41*, 91−101.
(10) Liu, H. K.; Ramachandran, E.; Chen, Y. H.; Chang, W. J.; Lii, K. H. High-Temperature, High-Pressure Hydrothermal Synthesis, Characterization, and Structural Relationships of Layered Uranyl Arsenates. *Inorg. Chem.* **2014**, *53*, 9065−9072.
(11) Piret, P.; Deliens, M. Vanmeersscheite uranium uranyl phosphate hydrate $U(UO_2)_3(PO_4)_2(OH)_6{\cdot}4H_2O$ and meta-vanmeersscheite $U(UO_2)_3(PO_4)_2(OH)_6{\cdot}2H_2O$, new minerals, *Bull. Mineral.***1982** *105*, 125−128.
(12) Demartin, F.; Diella, V.; Donzelli, S.; Gramaccioli, C. M.; Pilati, T. The importance of accurate crystal structure determination of uranium minerals. I. Phosphuranylite $KCa(H_3O)_3(UO_2)_7(PO_4)_4O_4[8H_2O]$. *Acta Crystallogr., Sect. B: Struct. Sci.* **1991**, *B47*, 439−446.
(13) Atencio, D.; Neumann, R.; Silva, A. J. G. C.; Mascarenhas, Y. P. Phurcalite from Perus, Sao Paulo, Brazil, and redetermination of its crystal structure. *Can. Mineral.* **1991**, *29*, 95−105.
(14) Bugaris, D. E.; zur Loye, H.-C. Materials discovery by flux crystal growth: Quartenary and higher oxides. *Angew. Chem., Int. Ed.* **2012**, *51*, 3780−3811.
(15) Morrison, G.; Smith, M. D.; zur Loye, H.-C. Understanding the Formation of Salt-Inclusion Phases: An Enhanced Flux Growth Method for the Targeted Synthesis of Salt-Inclusion Cesium Halide Uranyl Silicates. *J. Am. Chem. Soc.* **2016**, *138*, 7121−7129.
(16) Bruker. *APEX3, SAINT+, and SADABS*; Bruker AXS, Inc.: Madison, WI, USA, 2015.
(17) Sheldrick, G. M. SHELXT—Integrated space-group and crystal-structure determination. *Acta Crystallogr., Sect. A: Found. Adv.* **2015**, *A71*, 3−8.
(18) Sheldrick, G. M. Crystal structure refinement with SHELXL. *Acta Crystallogr., Sect. C: Struct. Chem.* **2015**, *C71*, 3−8.
(19) Dolomanov, O. V.; Bourhis, L. J.; Gildea, R. J.; Howard, J. A. K.; Puschmann, H. OLEX2: A complete structure solution. *J. Appl. Crystallogr.* **2009**, *42*, 339−341.
(20) Spek, A. L. Structure validation in chemical crystallography. *Acta Crystallogr., Sect. D: Biol. Crystallogr.* **2009**, *D65*, 148−155.
(21) Kubelka, P.; Munk, F. Z. Ein Beitrag Zur Optik Der Farbanstriche. *Z. Techn. Phys.* **1931**, *12*, 593−601.
(22) Glasser, L.; Jenkins, H. D. B. Volume-Based Thermodynamics: A prescription for its application and usage in approximating and predicting thermodynamic data. *J. Chem. Eng. Data* **2011**, *56*, 874−880.
(23) Glasser, L.; Jenkins, H. D. B. Predictive thermodynamics for ionic solids and liquids. *Phys. Chem. Chem. Phys.* **2016**, *18*, 21226−22140.
(24) Jenkins, H. D. B.; Roobottom, H. K.; Passmore, J.; Glasser, L. Relationships amoung Ionic Lattice Energies, Molecular (formula Unit) Volumes and Thermochemical Radii. *Inorg. Chem.* **1999**, *38*, 3609−3620.
(25) Yoder, C. H.; Flora, N. J. Geochemical applications of the simple salt approximation to the lattice energies of complex materials. *Am. Mineral.* **2005**, *90*, 488−496.
(26) Jenkins, H. D. B.; Glasser, L. Standard absolute entropy, S°_{298}, values from volume or density. *Inorg. Chem.* **2003**, *42*, 8702−8708.
(27) Konings, R. J. M.; Benes, O.; Kovacs, A.; Manara, D.; Sedmidubsky, D.; Gorokhov, L.; Iorish, V. S.; Yungman, V.; Shenyavskaya, E.; Osina, E. The thermodynamic properties of f-elements and their compounds. Part 2. The lanthanide and actinide oxides. *J. Phys. Chem. Ref. Data* **2014**, *43*, 0131101.
(28) Chase, M. W., Jr. *NIST−JANAF Thermochemical Tables, Fourth Edition Part I, Al-Co*; J. Physical and Chemical Reference Data, Monographs, Vol. 9; National Institutes of Standards and Technology (NIST): Gaithersburg, MD, USA, 1998.
(29) Han, J.; Goncharov, V.; Kaledin, L. A.; Komissarov, A. V.; Heaven, M. C. Electronic spectroscopy and ionization potential of UO_2 in the gas phase. *J. Chem. Phys.* **2004**, *120*, 5155−5163.
(30) Xu, C.; de Beer, E.; Neumark, D. M. Photoelectron spectroscopy of PO_2^-. *J. Chem. Phys.* **1996**, *104*, 2749−2751.
(31) Rosseinsky, D. R.; Glasser, L.; Jenkins, H. D. B. Thermodynamic clarification of the curious ferric/potassium ion exchange accompanying the electrochromic redox reactions of Prussian blue, iron(III) hexacyanoferrate(II). *J. Am. Chem. Soc.* **2004**, *126*, 10472−10477.
(32) Kresse, G.; Furthmuller, J. Efficient iterative schemes for *ab initio* total-energy calculations using a plane-wave basis set. *Phys. Rev. B: Condens. Matter Mater. Phys.* **1996**, *54*, 11169−11186.
(33) Kresse, G.; Furthmuller, J. Efficiency of ab-initio total energy calculations for metals and semiconductors using a plane-wave basis set. *Comput. Mater. Sci.* **1996**, *6*, 15−50.
(34) Perdew, J. P.; Burke, K.; Ernzerhof, M. Generalized Gradient Approximation Made Simple. *Phys. Rev. Lett.* **1997**, *78*, 1396−1399.
(35) Blochl, P. E. Projector augmented-wave method. *Phys. Rev. B: Condens. Matter Mater. Phys.* **1994**, *50*, 17953−17979.
(36) Kresse, G.; Joubert, D. From ultrasoft pseudopotentials to the projector augmented-wave method. *Phys. Rev. B: Condens. Matter Mater. Phys.* **1999**, *59*, 1758−1775.
(37) Anisimov, V. I.; Solovyev, I. V.; Korotin, M. A.; Czyzyk, M. T.; Sawatzky, G. A. Density-functional theory and NiO photoemission spectra. *Phys. Rev. B: Condens. Matter Mater. Phys.* **1993**, *48*, 16929−16934.
(38) Liechtenstein, A. I.; Anisimov, V. I.; Zaanen, J. Density-functional theory and strong interactions: Orbital ordering in Mott−Hubbard insulators. *Phys. Rev. B: Condens. Matter Mater. Phys.* **1995**, *52*, R5467−R5470.
(39) Schoenes, J. Recent specroscopic studies of UO_2. *J. Chem. Soc., Faraday Trans. 2* **1987**, *83*, 1205−1213.
(40) Kotani, A.; Yamazaki, T. Systematic Analysis of Core Photoemission Spectra for Actinide Di-Oxides and Rare-Earth Sesqui-Oxides. *Prog. Theor. Phys. Suppl.* **1992**, *108*, 117−131.
(41) Brincat, N. A.; Parker, S. C.; Molinari, M.; Allen, G. C.; Storr, M. T. Ab Initio Investigation of the UO_3 Polymorphs: Structural Properties and Thermodynamic Stability. *Inorg. Chem.* **2014**, *53*, 12253−12264.
(42) Colmenero, F.; Bonales, L. J.; Cobos, J.; Timon, V. Density Functional Theory Study of the Thermodynamic and Rama Vibrational Properties of γ-UO_3 Polymorph. *J. Phys. Chem. C* **2017**, *121*, 14507−14516.
(43) Casillas-Trujillo, L.; Baldinozzi, G.; Patel, M. K.; Xu, H.; Sickafus, K. E. Comparison of bonding and charge denisty in δ-UO_3, γ-UO_3, and La_6UO_{12}. *Phys. Rev. Mater.* **2017**, *1*, 065404.
(44) Wang, Z.; Zachara, J. M.; Gassman, P. L.; Liu, C.; Qafoku, O.; Yantasee, W.; Catalano, J. G. Fluorescence spectroscopy of U(VI)-silicates and U(VI)-contaminated Hanford sediment. *Geochim. Cosmochim. Acta* **2005**, *69*, 1391−1403.
(45) Cordfunke, E. H. P.; Ouweltjes, W. Standard enthalpies of formation of uranium compounds. XII. Anhydrous phosphates. *J. Chem. Thermodyn.* **1985**, *17*, 465−471.
(46) Holland, D.; Jenkins, H. B. D. An assessment of thermodynamic difference rule for mixed inorganic oxides and comments on the entalpies of formation of phosphates. *Thermochim. Acta* **2015**, *601*, 63−67.
(47) Drouet, C. A comprehensive guide to experimental and predicted thermodynamic properties of phosphate apatite minerals in view of applicative purposes. *J. Chem. Thermodyn.* **2015**, *81*, 143−159.
(48) To calculate the total energies of isolated alkali ions, we used a 20 Å × 20 Å × 20 Å cubic cell with an ion placed in the middle of the cell. We applied image-charge correction because the total energies converge faster as a function of the cell volume. The ions total energies were converged at the cell volume used.
(49) Goldschmidt, V. M. Crystal Structure and Chemical Constitution. *Trans. Faraday Soc.* **1929**, *25*, 253−283.

DOI: 10.1021/acs.inorgchem.8b00434
Inorg. Chem. XXXX, XXX, XXX−XXX